J|A|C|S ARTICLES

Published on Web 05/26/2009

Nascent Metal Atom Condensation in Self-Assembled Monolayer Matrices: Coverage-Driven Morphology Transitions from Buried Adlayers to Electrically Active Metal Atom Nanofilaments to Overlayer Clusters during Aluminum Atom Deposition on Alkanethiolate/Gold Monolayers

Masato M. Maitani,[†] Thomas A. Daniel,[‡] Orlando M. Cabarcos,[§] and David L. Allara*[,†,‡,§]

Department of Materials Science and Engineering, The Materials Research Institute, and Department of Chemistry, The Pennsylvania State University, University Park, Pennsylvania 16802

Received February 22, 2009; E-mail: dla3@psu.edu (DLA)

Abstract: Al atom deposition with controlled coverages has been carried out on self-assembled monolayers (SAMs), prepared by assembly of $HS(CH_2)_{15}X$, with X = $-CH_3$ (M-SAM) and $-CO_2CH_3$ (ME-SAM), on Au {111} substrates, and the resulting structures and electrical properties analyzed in situ by ultrahigh-vacuum, multiple mode atomic force microscopy (contact, noncontact, and conducting probe) and infrared reflection spectroscopy. The M−SAM data clearly reveal a distinct morphology transition at ∼3 Al atoms per adsorbate molecule (3 EL) from formation of a buried ∼1:1 Al−Au adlayer at low coverages to metal overlayer cluster nucleation and the appearance of isolated metal nanofilaments with varied behaviors including Ohmic conduction, resistive switching (*memristor*), and vestiges of quantum-like conductance steps. The ME-SAM data confirm our earlier report of a highly efficient, 1:1 chemical trapping of initial nascent Al atoms by the terminal ester group while also revealing formation of isolated, conducting filaments, mainly at SAM defects, and the presence of an insulating overlayer up to ∼5 EL. For both SAMs, despite the large thermochemical driving forces to exhaustively form inorganic products, subtle kinetic pathways guide the evolution of metal nanostructures within and contiguous to the SAM. Overall the experiments demonstrate a highly controlled, quantitative strategy for exploring the chemistry of nascent metal atoms with organic moieties as well as providing opportunities to generate novel metal nanostructures with significant implications for molecular and organic device applications.

1. Introduction

Top metal contacts play a critical role in organic electronic devices, including molecular electronic devices.[1−6] Metal vapor-phase deposition is a very common and efficient processing method for fabricating the top electrode with a wide range of possible metals, typically with controllable, uniform coverages. Thus, a fundamental understanding of the structure evolution for each type of metal and organic surface combination is important in designing large-scale production of layered organic electronic devices. This is of critical importance in molecular devices based on self-assembled monolayers (SAMs) in which the active device behavior is concentrated in a layer only one molecule in thickness, and the demands on sharp, clean contact interfaces with no metal atom leakage between contacts are extreme. There is a growing body of literature, however, that shows evidence of various detrimental effects including metal penetration, chemical reactions with the device molecules, and highly nonuniform metal cluster generation in and on the organic layer during vapor-phase deposition of metal.[7−41] These characteristics not only cause nonuniform contacts but can have large

† Department of Materials Science and Engineering.
‡ The Materials Research Institute.
§ Department of Chemistry.

(1) Mitschke, U.; Bauerle, P. *J. Mater. Chem.* **2000**, *10* (7), 1471–1507.
(2) Dimitrakopoulos, C. D.; Patrick, R. L.*Adv. Mater.* **2002**, *14* (2), 99–117.
(3) Horowitz, G. *Adv. Mater.* **1998**, *10* (5), 365–377.
(4) Mantooth, B. A.; Weiss, P. S. *Proc. IEEE* **2003**, *9* (11), 1785–1802.
(5) Chen, J.; Wang, W.; Klemic, J.; Reed, M. A.; Axelrod, B. W.; Kaschak, D. M.; Rawlett, A. M.; Price, D. W.; Dirk, S. M.; Tour, J. M.; Grubisha, D. S.; Bennett, D. W. *Ann. N. Y. Acad. Sci. (Mol. Electron. II)* **2002**, *960*, 69–99.
(6) Campbell, S. *J. Vac. Sci. Technol. A* **2003**, *21* (3), 521–531.
(7) Jung, D. R.; Czanderna, A. W. *Crit. Rev. Solid State Mater. Sci.* **1994**, *19*, 1–54.
(8) Ahn, H.; Whitten, J. E. *J. Phys. Chem. B* **2003**, *107*, 6565–6572.
(9) Ahn, H.; Zharnikov, M.; Whitten, J. E. *Chem. Phys. Lett.* **2006**, *428* (4−6), 283–287.
(10) Carlo, S. R.; Wagner, A. J.; Fairbrother, D. H. *J. Phys. Chem. B* **2000**, *104*, 6633–6641.
(11) Dannetun, P.; Boman, M.; Stafstrom, S.; Salaneck, W. R.; Lazzaroni, R.; Fredriksson, C.; Bredas, J. L.; Zamboni, R.; Taliani, C. *J. Chem. Phys.* **1993**, *99* (1), 664–672.
(12) deBoer, B.; Frank, M. M.; Chabal, Y. J.; Jiang, W.; Garfunkel, E.; Bao, Z. *Langmuir* **2004**, *20*, 1539–1542.
(13) Durr, A. C.; Schreiber, F.; Kelsch, M.; Carstanjen, H. D.; Dosch, H.; Seeck, O. H. *J. Appl. Phys.* **2003**, *93* (9), 5201–5209.
(14) Faupel, F.; Willecke, R.; Thran, A. *Mater. Sci. Eng., R* **1998**, *22* (1), 1–55.
(15) Fisher, G. L.; Hooper, A.; Opila, R. L.; Jung, D. R.; Allara, D. L.; Winograd, N. *J. Electron Spectrosc. Relat. Phenom.* **1999**, *98−99*, 139–148.
(16) Fisher, G. L.; Hooper, A. E.; Opila, R. L.; Allara, D. L.; Winograd, N. *J. Phys. Chem. B* **2000**, *104*, 3267–3273.

 10.1021/ja901376w CCC: $40.75 © 2009 American Chemical Society

effects on the interface electronic structure characteristics, as suggested by both experiment and theory.[6−9,13,28,36,39−47]

The study of metal vapor deposition on SAMs is useful both as an approach for direct understanding of molecular electronic devices with vapor deposited top contacts and as a fundamental method for gaining a detailed understanding of the chemistry and physics of nascent metal atom−molecule interactions with molecular groups. The latter is particularly interesting in the sense that upon initial approach and contact with the nascent metal atom at molecular moieties, the system is often very far from equilibrium with steep chemical potential gradients, especially for highly reactive metals, and the final chemical and physical state of the surface layers can be driven more by kinetic than thermodynamic paths. Such effects have been observed in previous studies which have utilized infrared spectroscopy (IRS),[7,12,15−17,19,21,30,31,33,34,37,41,43,46,48] photoemission spectroscopy (X-ray or UV generated),[7−10,15−20,29−31,33,34,37,41,47,48] secondary ion mass spectrometry,[15−17,19,22,23,31−34,37,46,48] scanning probe microscopies,[12,24,25,30,35,37,47] and near-edge X-ray absorption fine structure spectroscopy[41,47] to characterize the complex behaviors.

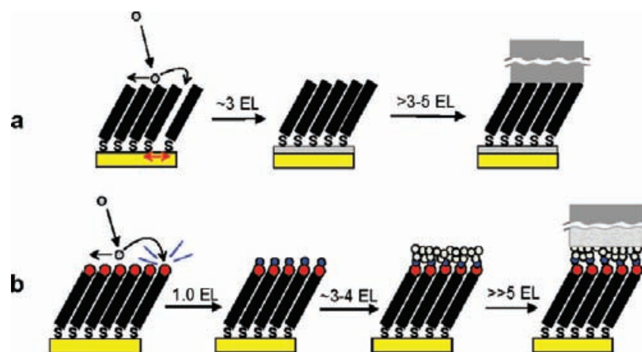

Figure 1. Schematics of the earlier reported Al deposition process and proposed mechanistic details for Al on (a) an inert M-SAM and (b) a reactive ME-SAM: (a) the steps (from left to right) show (a1) Al atoms striking the surface and diffusing into the SAM via a dynamic transient hole mechanism (see red arrow) to form a uniform Au/Al/S interface layer up to ∼2−3 EL coverage and (a2) formation of an Al overlayer; (b) the steps (from left to right) show (b1) 1:1 reaction with ester groups to form a uniform layer of a reduced ester group reaction product with no SAM penetration, (b2) nucleation and growth of a dielectric, organometallic Al layer consuming ∼3−4 additional EL of Al, and (b3) growth of a metallic overlayer in which the lower portion consists of an ∼3 nm, highly porous layer, whereas the top layer has a similar density to bulk Al metal. See text for details.

Of particular interest to us has been the case of Al deposition on the model systems of alkanethiolate SAMs on Au {111} for which we have shown that the intermediate reactivity of the nascent Al atoms, combined with a large degree of kinetic (vs thermochemical) control of reaction channels, leads to a wide variety of unexpected metal morphologies and reaction chemistry as a function of the specific substituent group at the alkyl chain terminus.[7,8,11,12,15−19,31,48] Two specific illustrative cases of the extreme limits of behavior are given by Al deposition on the methyl- and methyl ester-terminated hexadecanethiolate SAMs (M-SAM and ME-SAM, respectively),[19] as summarized pictorially in Figure 1. The M-SAM case shows a spectrum of deposition modes, including penetration to the Au/SAM interface and ambient surface overlayer formation.[19] The penetration was explained in terms of Al atoms diffusing into dynamically formed temporal vacancies in the SAM caused by lateral, short-range excursions (essentially nearly uncorrelated vibrations) of the Au−thiolate moieties around their equilibrium positions on the Au substrate.[49,50] Once Al atoms penetrated to the substrate, energetically favorable Al insertion into S−Au bonds could occur, resulting in strongly decreased lateral positional fluctuations, thereby shutting off the temporal vacancy channels. It was also reported that Al penetration can be avoided by introducing reactive functional groups such as -CO_2H, -CH_2OH,

(17) Fisher, G. L.; Walker, A. V.; Hooper, A. E.; Tighe, T. B.; Bahnck, K. B.; Skriba, H. T.; Reinard, M. D.; Haynie, B. C.; Opila, R. L.; Winograd, N.; Allara, D. L. *J. Am. Chem. Soc.* **2002**, *124*, 5528–5541.
(18) Haynie, B. C.; Walker, A. V.; Tighe, T. B.; Allara, D. L.; Winograd, N. *Appl. Surf. Sci.* **2003**, *203−204*, 433–436.
(19) Hooper, A.; Fisher, G. L.; Konstadinidis, K.; Jung, D.; Nguyen, H.; Opila, R.; Collins, R. W.; Winograd, N.; Allara, D. L. *J. Am. Chem. Soc.* **1999**, *121*, 8052–8064.
(20) Konstadinidis, K.; Zhang, P.; Opila, R. L.; Allara, D. L. *Surf. Sci.* **1995**, *338* (1−3), 300–312.
(21) Nagaoka, S.; Matsumoto, T.; Okada, E.; Mitsui, M.; Nakajima, A. *J. Phys. Chem. B* **2006**, *110*, 16008–16017.
(22) Nagy, G.; Walker, A. V. *J. Phys. Chem. B* **2006**, *110*, 12543–12554.
(23) Nagy, G.; Walker, A. V. *J. Phys. Chem. C* **2007**, *111*, 8543–8556.
(24) Ohgi, T.; Sheng, H.-Y.; Nejoh, H. *Appl. Surf. Sci.* **1998**, *130−132*, 919–924.
(25) Ohgi, T.; Sheng, H.-Y.; Dong, Z.-C.; Nejoh, H. *Surf. Sci.* **1999**, *442* (2), 277–282.
(26) Peisert, H.; Knupfer, M.; Schwieger, T.; Fink, J. *Appl. Phys. Lett.* **2002**, *80* (16), 2916–2918.
(27) Seki, K.; Tani, T.; Ishii, H. *Thin Solid Films* **2007**, *273*, 20–26.
(28) Shen, C.; Kahn, A.; Schwartz, J. *J. Appl. Phys.* **2001**, *89* (1), 449–459.
(29) Tarlov, M. J. *Langmuir* **1992**, *8*, 80–89.
(30) Tighe, T. B.; Daniel, T. A.; Zhu, Z.; Uppili, S.; Winograd, N.; Allara, D. L. *J. Phys. Chem. B* **2005**, *109*, 21006–21014.
(31) Walker, A. V.; Tighe, T. B.; Cabarcos, O. M.; Reinard, M. D.; Haynie, B. C.; Uppili, S.; Winograd, N.; Allara, D. L. *J. Am. Chem. Soc.* **2004**, *126*, 3954–3963.
(32) Walker, A. V.; Tighe, T. B.; Stapleton, J.; Haynie, B. C.; Uppili, S.; Allara, D. L.; Winograd, N. *Appl. Phys. Lett.* **2004**, *84* (20), 4008–4010.
(33) Walker, A. V.; Tighe, T. B.; Haynie, B. C.; Uppili, S.; Winograd, N.; Allara, D. L. *J. Phys. Chem. B* **2005**, *109*, 11263–11272.
(34) Walker, A. V.; Tighe, T. B.; Cabarcos, O.; Haynie, B. C.; Allara, D. L.; Winograd, N. *J. Phys. Chem. C* **2007**, *111*, 765–772.
(35) Wang, B.; Xiao, X.; Sheng, P. *J. Vac. Sci. Technol. B* **2000**, *18*, 2351–2358.
(36) Watkins, N. J.; Yan, L.; Gao, Y. *Appl. Phys. Lett.* **2002**, *80* (23), 4384–4386.
(37) Zhu, Z.; Daniel, T. A.; Maitani, M.; Cabarcos, O. M.; Allara, D. L.; Winograd, N. *J. Am. Chem. Soc.* **2006**, *128*, 13710–13719.
(38) Herdt, G. C.; Jung, D. R.; Czanderna, A. W. *Prog. Surf. Sci.* **1995**, *50* (1−4), 103–129.
(39) Lai, Y. S.; Tu, C. H.; Kwong, D. L.; Chen, J. S. *Appl. Phys. Lett.* **2005**, *87* (12), 122101–122103.
(40) Tu, C. H.; Lai, Y. S.; Kwong, D. L. *Appl. Phys. Lett.* **2006**, *89* (6), 062105–3.
(41) Wacker, D.; Weiss, K.; Kazmaier, U.; Woll, C. *Langmuir* **1997**, *13*, 6689–6696.
(42) Crispin, X.; Geskin, V.; Crispin, A.; Cornil, J.; Lazzaroni, R.; Salaneck, W. R.; Bredas, J. L. *J. Am. Chem. Soc.* **2002**, *124*, 8131–8141.
(43) Lenfant, S.; Guerin, D.; TranVan, F.; Chevrot, C.; Palacin, S.; Bourgoin, J. P.; Bouloussa, O.; Rondelez, F.; Vuillaume, D. *J. Phys. Chem. B* **2006**, *110*, 13947–13958.
(44) Ovchenkov, Y. A.; Geisler, H.; Burst, J. M.; Thornburg, S. N.; Ventrice, C. A.; Zhang, C.; Redepenning, J.; Losovyj, Y.; Rosa, L.; Dowben, P. A.; Doudin, B. *Chem. Phys. Lett.* **2003**, *381* (1−2), 7–13.
(45) Pesavento, P. V.; Chesterfield, R. J.; Newman, C. R.; Frisbie, D. *J. Appl. Phys.* **2004**, *96* (12), 7312–7324.
(46) Rousseau, R.; DeRenzi, V.; Mazzarello, R.; Marchetto, D.; Biagi, R.; Scandolo, S.; delPennino, U. *J. Phys. Chem. B* **2006**, *110*, 10862–10872.
(47) Tai, Y.; Shaporenko, A.; Noda, H.; Grunze, M.; Zharnikov, M. *Adv. Mater.* **2005**, *17* (14), 1745–1749.
(48) Walker, A. V.; Tighe, T. B.; Reinard, M. D.; Haynie, B. C.; Allara, D. L.; Winograd, N. *Chem. Phys. Lett.* **2003**, *369* (5−6), 615–620.
(49) Bhatia, R.; Garrison, B. J. *Langmuir* **1997**, *13*, 765–769.
(50) Bhatia, R.; Garrison, B. J. *Langmuir* **1997**, *13*, 4038–4043.

and -CO_2CH_3,[7,8,11,12,15−19,31,48] thereby yielding a more precise Al/SAM/Au layered structure.[19] The proposed deposition mechanism, however, was based on characterization data from probes (infrared reflection spectroscopy (IRS), X-ray photoelectron spectroscopy (XPS), time-of-flight secondary-ion mass spectrometry (ToF-SIMS), spectroscopic ellipsometry) that only provided an average behavior of large areas (macro to >1 μm) with no local information at the atomic/molecular level across the surfaces and, in general, with only qualitative conclusions. In particular, evidence for penetration of Al atoms to the interface in the case of the M-SAM was based solely on the appearance of cluster species in the ToF-SIMS spectra with only a qualitative estimate of the coverage of penetrated atoms and their spatial distribution. Recently we have shown that conducting probe AFM (cp-AFM) is a very useful tool for tracking subtleties in the morphology of the deposited metal atom; e.g., in the case of Au deposition it was possible to discern the formation of Au filaments which cannot be directly detected by XPS, Tof-SIMS, and IRS spectroscopic measurements.[37] The cp-AFM probe was able to image simultaneously both the topography and electrical current, clearly revealing the positional dependence of conducting Au filaments relative to the substrate structure.

In this new study, we have utilized a combination of cp-AFM, contact mode AFM (c-AFM), and noncontact mode AFM (nc-AFM) to directly probe the local nanoscale topographic and electrical characteristics of Al films formed by controlled vapor deposition onto alkanethiolate SAMs on Au {111}. The nc-AFM mode was included in order to noninvasively image surface metal clusters which could otherwise be dislodged or swept by direct contact with the tip. We further carried out highly quantitative IRS measurements in order to track chain orientations, molecular conformations, and coverages during the depositions. We apply these probes to the cases of Al deposition on the chemically inert $H_3C(CH_2)_{15}S$-/Au{111} SAM (M-SAM) and the reactive $H_3CO_2C(CH_2)_{15}S$-/Au{111} (ME−SAM) surfaces to look for clear differences in terms of the metal film growth as a function of Al coverage and thus test the previously proposed deposition mechanism. In particular the focus for the M-SAM was to look for distinctive, coverage-dependent transitions between (1) Al penetration into the Au/SAM interface and (2) Al deposition onto the top of SAM. On the other hand, for the ME-SAM case, in which every molecule terminal group undergoes chemical reaction with Al atoms, the focus was to look at the uniformity of the rapidly formed top overlayer and to check for any formation of electrically conducting metal filaments which would have gone undetected by our previous characterization probes. The issue of metal filaments was of particular interest both for the relevance to the electrical integrity of molecular electronic devices as well as for the detailed conductance characteristics that could be exhibited by atomic-scale metal atom “strings” or wires.

At the simplest level, the results of our present study fully support our previously proposed mechanism, but also add new, critical details. In the case of the M-SAM the data reveal the existence of three distinct, sequential stages in the metal deposition as a function of increasing coverage (θ in Al atoms per SAM molecule): (1) penetration to the substrate ($\theta = 0$ to ~ 3), (2) intermediate filament generation (($\theta = \sim 2$ to ~ 5), and (3) top deposition stage (($\theta > 5$). In the intermediate stage, filaments protruding up from the substrate appear uniformly across the surface to provide electrical short-circuit paths to the Au substrate. In the case of the ME−SAM the top deposited metal film remains smooth in all stages, and in the early stages no conducting filaments are observed. At higher coverages, in spite of the high reactivity of the ester groups for the Al atoms, small fractions of the surface showed eventual appearance of filaments, primarily at step edges of the Au substrate where some disorder in the SAM is expected. These results show that for well-formed SAMs, even for those with a highly reactive terminal group, electrical shorts can occur. A careful study of the electrical properties of the filaments in the M-SAM show that they undergo a variety of fluctuating behaviors under voltage bias including filament breakdown (fuse effects), switching, and memory. These behaviors indicate voltage induced electromigration of metal, rather than molecular characteristics in the junction. Finally, given the conservation of the adsorbate molecules in the SAM during deposition and the invariance of the tilt angles (from IRS), the filaments appear to be limited exclusively to formation in static defects in the SAM. Thus, the filament diameters are limited to no more than a few atoms, representing a near limit in formation of Al wires. Electrical measurements further indicate that the conductances are perhaps several orders of magnitude below that of bulk aluminum and also well below the quantum conductance limit. These data clearly show that the onset of filament formation in metal/organic contacts can give rise to spurious electrical behavior that could be mistakenly attributed to molecular device effects.

2. Experimental Section

2.1. Self-Assembled Monolayer Preparation. Previoulsy reported procedures[51−53] were followed. Substrates consisted of Au/mica (Agilent/Molecular Imaging, Tempe, AZ) and thermally deposited Au (~200 nm) on oxide covered Si(100) wafers or quartz crystal microbalance (QCM; convex highly polished QCM, Cold Springs R&D, Syracuse, NY; rms roughness, 0.1−0.2 nm) substrates. The Au/mica and Au/Si(oxide) substrates were used for AFM and in situ IRS experiments, respectively. The QCM crystals were used to follow the exact amount of Al deposited on the nearby sample. Since in the case of the M-SAM the sticking coefficient is not unity, the QCM gold electrode surfaces were coated with the M-SAM such that the sticking coefficient would be identical for the QCM and sample, thus giving accurate Al coverages corrected for the scattering. The thermally deposited Au surface was prepared on Si and QCM substrates covered with Cr (~10 nm) as an adhesive layer (Cr and Au were deposited consecutively under a base pressure of $\sim 2 \times 10^{-8}$ Torr) at room temperature. Hydrogen flame annealed Au on mica and freshly deposited Au surfaces were immediately immersed into the 0.1 mM thiol solution in pure dichloromethane. After immersion for 12 h in the solution at room temperature, samples were removed from solution, rinsed with dichloromethane and ethanol, dried under a purified N_2 flow, and then loaded into the ultrahigh-vacuum (UHV) chamber of either the AFM or IRS. The IRS spectra and AFM lattice images confirmed the quality of the SAMs for each experiment.

2.2. Metal Deposition Procedure. Deposition was carried out for both the AFM and the IRS experiments using resistively heated tungsten coils loaded with Al pellets (99.999%, Kurt J. Lesker, PA). The coils were heated using a direct current (dc) power supply (GEN6-200, Lambda, NJ), and the deposition rate was controlled at a rate of 0.077 atoms$\cdot$nm$^{-2}\cdot$s^{-1} (4.6 atoms$\cdot$nm$^{-2}\cdot$min^{-1}, equivalent to 1 (atom/molecule)/min). A QCM crystal (SQM-160; maximum error, ±7%; Sigma Instruments, Fort Collins, CO) was

(51) Widrig, C. A.; Alves, C. A.; Porter, M. D. *J. Am. Chem. Soc.* **1991**, *113*, 2805–2810.
(52) Nuzzo, R. G.; Korenic, E. M.; Dubois, L. H. *J. Chem. Phys.* **1990**, *93* (1), 767–773.
(53) Nuzzo, R. G.; Dubois, L. H.; Allara, D. L. *J. Am. Chem. Soc.* **1990**, *112*, 558–569.

mounted adjacent to the sample so that the metal vapor flux would be nearly identical on both surfaces. To ensure complete accuracy. a geometric tooling factor was determined to correct for any slight differences in flux striking the sample and QCM surfaces and the actual amounts on each surface determined by thick film deposition and AFM measurements of step heights for masked areas. The QCM gold electrode surface also was covered with the same SAM as the sample in order to correct for a nonunity sticking coefficient ($S < 1$) on the sample surface. In the case of the ME-SAM the sticking coefficient was exactly 1.0 within error while for the M-SAM $S = 0.4 \pm 0.05$.

2.3. AFM Instrumentation. The experiments were performed in a UHV analysis chamber (base pressure < 5 × 10^{-10} Torr) connected to a metal deposition fore chamber with an intervening gate valve for isolation. The analysis chamber was configured with an RHK 350 scan head, RHK SPM 100 electronics system, and PLL Pro AFM controlling electronics system (RHK Technologies, Troy, MI). Silicon cantilevers (PPP-FMR; spring constant ∼ 2.8 N/m; tip radius ∼ 10 nm; Nanosensors, Neuchâtel, Switzerland), electronically conducting platinum−iridium (90:10) coated Si cantilevers (PPP-EFM; spring constant ∼ 3.0 N/m; tip radius, 20 nm; Nanosensors), and silicon cantilevers (SSS-NCHR; spring constant ∼ 40 N/m; tip radius, 2 nm; resonance frequency ∼ 330 kHz; quality factor ∼ 30 k; Nanosensors) were used for c-AFM, cp-AFM, and nc-AFM, respectively. Three different modes, c-AFM, cp-AFM, and nc-AFM, were utilized to obtain molecular lattice images, simultaneous topographic and tip−substrate current images, and topographic images, respectively. Molecular lattice images were taken by c-AFM frictional force imaging based on the stick and slip motion of the cantilever with a constant applied normal force. Contact mode with silicon tips was used for topography alone while conducting metalized tips were used for simultaneous topography and electrical current images. Typical contact images were recorded by bringing the tip into contact and then adjusting the force loading between −10 and +5 nN for the frictional force imaging and at +5 nN for cp-AFM imaging. The scan rate was varied from 50 to 200 nm·s^{-1} for the frictional force imaging and was fixed at 1 m·s^{-1} for cp-AFM imaging. For the topography−current scans the conducting tip was held at selected bias voltages relative to the Au substrate (grounded to the entire sample stage), allowing simultaneous maps of the electrical currents and topographic features. For $I-V$ sweeps the tip was placed at an arbitrary location in a region of interest and held there while the bias voltage was cycled through selected ranges. Since contact mode does not give accurate topography with deposited metal overlayers due to frictional wearing of the soft Al metal surface by the hard silicon tip, more accurate topography was obtained in separate experiments using nc-AFM in which the tip does not actually contact the surface. The nc-AFM mode was carried out by using a frequency-modulation (FM) feedback system (typically $\Delta f \sim -40$ Hz; constant amplitude ∼ 105 nm; scan rate ∼ 200 nm/s). For z and $x-y$ directions, the scan head was calibrated using Au single step edges (height, 0.3 nm) and the lattice constant of a hexadecanethiolate SAM on Au{111} surface (lattice constant, 0.5 nm), respectively[51,52] Sample images were determined as consistent results with images at three different locations for each experiment and at least three individual experiments for each experimental condition. All AFM images were taken within 5 h in order to avoid oxidation of the metal and relaxation of freshly formed metal film features. Further, the cp-AFM was done immediately after metal deposition to avoid formation of insulating oxide layers.

2.4. AFM Experimental Procedures. The AFM experiment consists of imaging in UHV before and after metal deposition. Each metal coverage was done in a separate experiment in order to minimize any buildup of impurities on consecutive growth surfaces. The freshly cleaned SAMs were loaded into the UHV chamber on the sample transfer arm immediately after reaching the base pressure range (<5 × 10^{-10} Torr), imaged by c-AFM, nc-AFM, and cp-AFM to confirm if the SAM surfaces had a well-ordered structure with the correct lattice parameters, were uniformly insulating and were free of critical defects such as particles. The samples were then transferred in vacuo into the metal deposition fore chamber, pumped by a turbo pump, and the fore chamber gate valve closed to isolate it from the main chamber. The sample was turned with the face opposite the source. Once the pressure reached the standard base value (∼1 × 10^{-8} Torr) the source was heated to produce a steady Al flux of the desired value, the sample rotated to face the source and amount of metal deposited monitored by the adjacent QCM crystal. During deposition the pressure rose to values <3 × 10^{-7} Torr. After reaching the desired coverage, the sample was rotated away from the source and the source turned off. Once theh fore camber pressure recovered to <4 × 10^{-8} Torr (several minutes), the sample was transferred into the analysis chamber and the gate valve closed. After the main chamber reached the base pressure range the sample was analyzed by the selected AFM mode.

2.5. IRS Experiments. The analysis was performed in a single UHV chamber pumped by a combination of turbo and ion pumps (base pressure < 3 × 10^{-7} Torr). The details have been presented in an earlier report.[19] The final spectra were determined as −log (R/R_0), where R is the sample spectrum and R_0 is the spectrum of a $C_{16}D_{33}S$/Au{111} SAM taken before and again after the deposition run. These two reference spectra were compared to ensure that the instrument and optics had remained constant throughout the deposition experiment.

2.6. Definition of Metal Coverage. The metal coverage was determined directly from the oscillation frequency shift of the calibrated (geometry tooling factor correction for sample placement) QCM crystal next to the sample by means of the Sauerbrey equation,[54] which yields the deposited mass per unit area. For convenience in interpretation of the data in molecular terms, the coverage (θ) is reported in terms of the number of deposited metal atoms per molecule in the SAM, designated as an equivalent layer (EL). Since an ideally densely packed M-SAM on a Au(111) substrate contains 4.6 molecules·nm^{-2}, this value would represent the Al atom coverage for $\theta = 1$. The use of the SAM coated QCM crystal electrodes eliminates errors for sticking coefficients < 1.

3. Results

3.1. Topographic and Electrical Conduction Images of the Initial SAMs. AFM images of bare M- and ME-SAMs on a Au/mica substrate are shown in Figures 2 and 3, respectively. Topographic images of a bare M-SAM surface were taken by cp-AFM (1 μm × 1 μm scan range) and nc-AFM (0.4 μm × 0.4 μm scan range), as shown in Figure 2a,d, respectively. Topographic c-AFM (1 μm × 1 μm) and nc-AFM (0.15 μm × 0.15 μm) images of a bare ME-SAM are shown in Figure 3a,d, respectively. Images for both SAMs reveal terraces and step edges of the underlying Au{111} substrate, which ensures that there are no problematic features such as particles, large area defects, or other contaminations on the initial surface. Topographic images of both SAMs taken by nc-AFM reveal detailed features of defects and domain boundaries of the SAM, which cannot be observed by contact modes where tip-induced contact interactions obscure subtle features as well as sweep loosely bound nanoparticles and contaminants away from the imaging area. The nc-AFM image of an ME-SAM (Figure 3d) shows the presence of nanoparticles, likely due to scattered contamination or clustered SAM precursor molecules that are not removed, even with very careful and thorough solvent rinsing. Careful topographic observation consistently shows that there are relatively more particles or clustered molecules, especially at step edges, for the ME-SAM compared to the lower surface energy M-SAM. Similar surface contamination was previously

(54) Sauerbrey, G. *Z. Phys.* **1959**, *155*, 206–222.

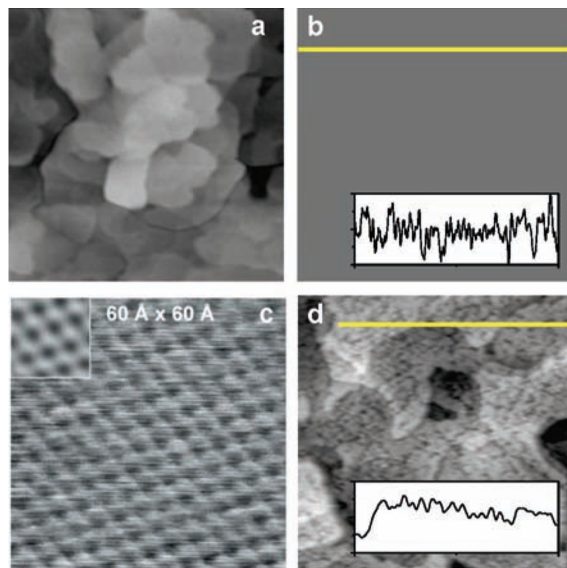

Figure 2. AFM images of a bare M-SAM: (a and b) simultaneous topographic and current images (1 μm × 1 μm); (c) frictional force (stick and slip) mode lattice image (6 nm × 6 nm, with high resolution in upper left inset); (d) nc-AFM topographic image (0.4 μm × 0.4 μm). The topographic images show the terraces and step edges of the underlying Au{111} substrate. The current image (b), taken with a probe bias of −10 mV applied to the substrate with a grounded tip, shows uniform insulator behavior across the surface within ±20 pA (±2.5 pA preamp limit), as shown in a line scan in the b inset (full scale, ±2 pA). The contact lattice image (c) exhibits the expected ($\sqrt{3} \times \sqrt{3}$) pattern (magnification shown in inset). The line scan inset in d is ±1 nm full height scale.

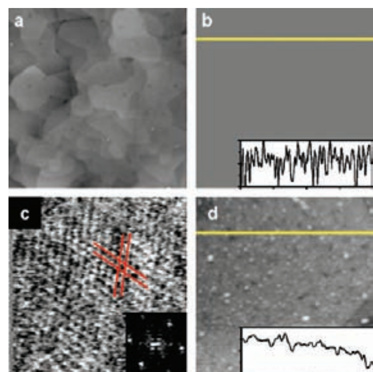

Figure 3. AFM images (1 μm × 1 μm) of the bare ME-SAM. Images a and b are simultaneously recorded topographic (c-AFM) and current (cp-AFM) images, respectively. The current image was taken with a −10 mV bias applied to the substrate with a grounded tip. This image shows insulator character within a ±20 pA current range (preamp noise, ±2.5 pA) with a line scan shown in the inset (yellow trace; full scale, ±2 pA). Images c and d are lattice and topographic images [(10 nm × 10 nm) and (0.15 μm × 0.15 μm), respectively] recorded using frictional force mode (c-AFM) and nc-AFM, respectively. The inset in d shows a topography line scan (yellow trace; full scale, ±1 nm). The topography images show the terraces and step edges of the underlying Au{111} substrate. The lattice image (c) shows the ($\sqrt{3} \times \sqrt{3}$) commensurate ad-layer on a Au(111) terrace (red lines mark the lattice directions; 2D FFT image in the inset).

observed on carboxylic acid terminated alkanethiolate/Au SAMs, where some contaminants are so strongly bound that typical contact mode forces are not sufficient to sweep them across the surface.[37]

Electrical current images, taken at a +10 mV tip bias simultaneously with the cp-AFM topographic images (Figures 2b and 3b for the M- and ME-SAMs, respectively), show that both SAMs are completely insulating across the surface within the current detection limit (±2.5 pA; noise level is shown in the figure inset). A low-voltage bias (10 mV) was chosen to minimize current-induced perturbations to the metal nanostructures but be sufficient to probe for short-circuit regions after metal deposition.

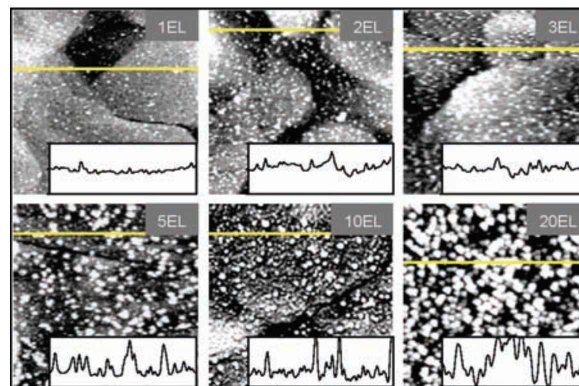

Figure 4. Topographic nc-AFM images (0.4 μm × 0.4 μm) of Al deposition on M-SAM samples at selected Al coverages from 1 to 10 EL. Insets show line scans (yellow lines; full scale, 1−5 EL, ±3 nm, and 10−20 EL, ±5 nm).

High-resolution contact mode lattice images (10 nm × 10 nm) of both SAMs (see Figures 2c and 3c, respectively) reveal the expected commensurate ($\sqrt{3} \times \sqrt{3}$) structure with a 5.0 ± 0.5 Å lattice constant (2D-FFT patterns in the inset, calculated from the whole image), within error of the ideal 4.99 Å value.[51,52] Inspection of the images shows a less sharp lattice image and a relatively distorted 2D-FFT pattern for the ME-SAM compared to the M-SAM. These results are consistent with the larger size and unsymmetrical character of the -CO_2CH_3 terminal group, which would be expected to lead to some surface disorder relative to the case of the CH_3 end group.

3.2. Al Deposition on the M-SAM. 3.2.1. Evolution of Topography via Noncontact Mode Imaging. Noncontact topographic images (0.4 μm × 0.4 μm) of the M-SAM with 0, 1, 2, and 3 EL of Al deposited are shown in Figure 4. In the initial deposition stage (∼1−3 EL), scattered height variation features are observed which can be associated with formation of occasional Al clusters on the surface, or possibly below the surface. These features increase in number and size with increasing Al coverage. Note, however, that they only constitute a minor fraction of the deposited metal up to ∼3 EL. For example, at 3 EL coverage if all Al atoms were located at the ambient SAM interface each of the protruding features on average would need to be at least 2 nm in height to account for all the metal (Al diameter ∼ 2.8 Å), whereas the heights of the bigger clusters are typically a few angstroms, from which we estimate only ∼0.1−0.5% of the deposited Al is incorporated in cluster form. While these noncontact images alone do not show whether the clusterlike features are located at the vacuum interface or the substrate interface or even imbedded in the SAM matrix, contact mode imaging, however, does reveal that the features are dominantly at the vacuum/SAM interface (see next section).

3.2.2. Contact Mode AFM Characterization of Lattice Order Degradation with Increasing Al Coverage. Contact mode lattice images (6 nm × 6 nm) of the M-SAM with 0, 1, 2, and 3 EL of deposited Al are shown in Figure 5. A typical spot on the bare SAM shows the expected ($\sqrt{3} \times \sqrt{3}$), R30° adlayer lattice. Regions with sharper lattice images were found (e.g., see Figure 3), but the translational order for the bare ME-SAM

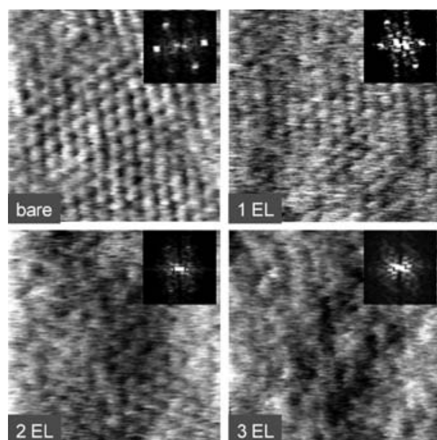

Figure 5. Contact mode lattice images (6 nm × 6 nm) of deposited Al at different coverages, as shown, on M-SAMs (2D FFT patterns in insets). After scanning each Al-covered sample, the tip quality was verified by imaging a new, bare SAM with observation of the expected lattice pattern.

in Figure 5 serves as a typical case that can be compared to the regions imaged with Al deposited. As the deposition amount increases from 1 to 3 EL, the lattice structures increasingly degrade, clearly seen in both the real space and FFT patterns, until at 3 EL the lattice barely is observable. Above 3 EL lattice images were no longer observed (data not shown). Since the cluster type features observed with nc-AFM (Figure 4) are not seen in the contact images, it is clear that in contact mode the AFM tip is sweeping Al clusters out of the scan area to leave a bare lattice image. From this we conclude that the clusters are located at the vacuum interface of the SAM.[55] Further, the continued ability to see a lattice up to 3 EL coverage shows that the fraction of Al atoms that had penetrated to the Au/S interface are indeed uniformly distributed laterally across the surface, as proposed in our earlier study.[19]

3.2.3. IRS Characterization of Alkyl Chain Conformational Disordering with Increasing Al Coverage. Further details of the coverage-disordering trend are given by in situ IRS data for the C−H stretching region of the spectrum of the M-SAM as a function of Al coverage (Figure 6). The peak assignments have been described previously.[52,53] Referring back to the AFM results, the IRS spectra overall are unaffected to any significant extent by the presence of either the small surface Al clusters or the presence of a Au/SAM Al interlayer. The main effects consist of minor broadening of the CH_2 C−H antisymmetric stretching mode feature at ~2918 cm^{-1} ($\nu^a_{CH_2}$). This feature, in particular, is quite sensitive to the extent of conformational order of the alkyl chain in the SAM. The full width at half-maximum (fwhm) values of this peak were extracted from peak fitting with mixed Gaussian and Lorentzian functions and plotted as a function of increasing metal coverage in Figure 6b, along with other peak widths for comparison. The fwhm of the peaks strongly increase to ~4 EL of Al deposition and subsequently tend to level off. Looking at the diagnostic $\nu^a_{CH_2}$ mode, the peak broadening signifies an increase in the gauche defect content

(55) As the sweeping process proceeds the tip will pick up Al debris and cause the tip radius to increase, thereby lowering the spatial resolution (initial radius curvature < 10 nm). Consequently, the lattice image degradation with coverage could be due in part to a tip effect. This effect was eliminated as a major contribution by observing that the same tip after sweeping was able to detect the ($\sqrt{3} \times \sqrt{3}$) lattice pattern on a new bare SAM (see Supporting Information).

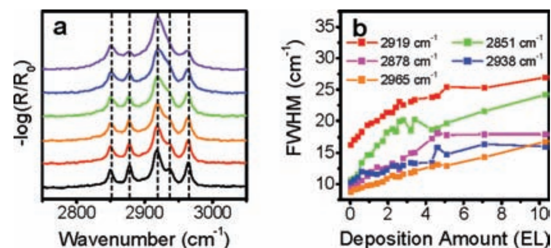

Figure 6. In-situ IRS spectra (a) and fwhm of each peak (b) of Al deposited M-Au SAM with continuing doses of Al up to ~10 EL. The mode assignments for the initial SAM are (frequencies in cm^{-1}): 2965, CH_3 C−H asym str ($\nu^a_{CH_3}$); 2958 CH_3 C−H asym str; 2938 CH_3 C−H sym str; 2919 CH_2 C−H antisym str; 2878 CH_3 C−H sym str; 2851 CH_2 C−H sym str.[52,53] Graph b contains the key to the color codes for the plots in a.

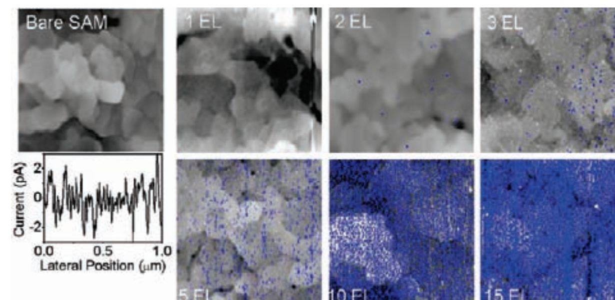

Figure 7. Topographic and current images (1 μm × 1 μm) of selected Al deposition coverages from 1 to 15 EL taken by cp-AFM. Current images are superimposed on the simultaneously recorded topographic images with the blue spots indicating short-circuit spots detected for a 10 mV bias applied between the conducting probe and the Au substrate of the SAM. The current line scan shown below the bare SAM image is at the noise level of the preamplifier and demonstrates the insulating character of the bare SAM. All images were taken on the third scan for consistency (see text).

in the chain assembly, which in turn would arise from decreases in the order of the packing arrangements of the chains both from horizontal and vertical displacements from the ideal lattice positions. The leveling off of the mode intensities, in particular for $\nu^a_{CH_2}$, above 4−5 EL coverages implies that continued nucleation and growth of Al clusters on the top surface have negligible effects on the conformational order of the chains buried under the metal overlayer. Since both the AFM and IRS data support constant adsorbate coverage with Al deposition, we conclude that the decay in conformational ordering arises from a decay in the order of the -S pinning lattice as it shifts from Au(111) to the Al/Au(111) adlayer.

3.2.4. Onset of Electrical Shorts at ~3 EL Al and Correlation with Surface Cluster Nucleation. Somewhat synchronously with the collapse of the translational order of the M-SAM lattice as increasing Al coverage approaches ~3 EL, the onset of electrical shorts appears, as seen by superimposed cp AFM topographic and current images (1 μm × 1 μm) in Figure 7. Short-circuit points (blue spots) between the grounded tip and the substrate (10 mV bias) are absent until 2 EL, where a few isolated spots appear, emerge uniformly at 3 EL, and are profusely distributed at higher coverages. Continued scanning of the surfaces results in the tip sweeping clusters away from the image region and a slow decrease in the surface density of short points. To allow consistent comparisons, the images shown in the figure were all taken on the third scan, at which point most of the clusters had been removed. Images at one scan with accurate cluster features are shown in the next section.

Scans of the initial and the 1 EL Al SAM surfaces show only insulating behavior. At the onset of shorts in the 2 EL image,

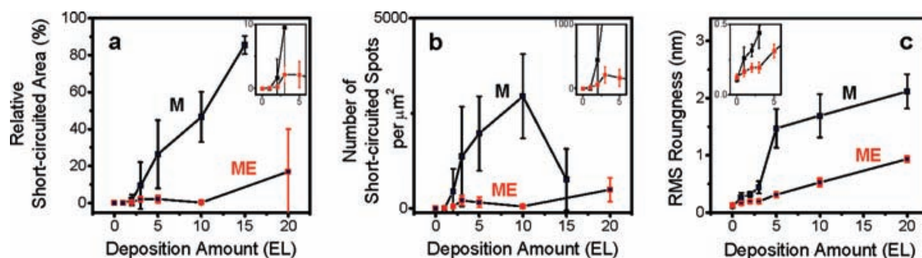

Figure 8. Plots of the relative short-circuited areas (a), number of shorts per μm^2 (b), and rms roughness of surfaces (c) as a function of the amount of Al deposition for data from the current images in Figure 7 and from averaged line scans (data not shown) across the nc-AFM images in Figure 4, respectively. The curves are labeled M and ME to designate the respective SAM. In counting the fraction of the area covered by shorts, a current ≥ 0.1 nA was used to define a short. The rms roughness values were determined from an average of line scans taken in 10 different spots. Only terrace regions were selected in order to remove effects of the substrate grain boundaries. The insets show magnified regions around ∼3 EL.

they appear mostly at typical SAM defects (Au substrate vacancy islands, Au substrate step edges, SAM structural domain boundaries, and different types of SAM disorder regions), but some appear in terrace regions. Examining the 3 EL Al image in detail, the generally smooth surfaces together with the contact mode evidence for some degree of remaining lattice ordering (see Figure 5) indicate that the shorts arise from conducting Al filaments, as opposed to open regions in the SAM where the tip could penetrate to direct contact with the substrate or approach closely enough for tunneling to reach the current threshold. Further, there is no strict correlation between topographic cluster features and filament shorts. For example, in the 3 EL coverage image, not all of the scattered cluster defects (white dots) show shorting behavior.

At the higher Al coverages the filament surface density greatly increases with shorts appearing uniformly across the surface. At this point the SAM lattice order has been degraded (see Figure 5), so molecular scale defects exist in all regions, including terraces. Note, however, that it is not possible from these data to know if the shorting at any given point occurs directly from the contact point to ground or via some lateral pathway below the SAM surface. Further, since the cp-AFM tip radius of curvature in our experiments ranges from ∼10 to 50 nm (depending somewhat on whether or not Al metal has been picked up in the scans), the actual filament diameters are likely *significantly smaller* than measured from the images.[56]

The shorting point distribution statistics are summarized in Figure 8a,b by plots of the percent of the image surface areas covered by shorts and the number of shorts per unit area. Figure 8c further shows the transition in the root mean square (rms) roughness of the surfaces (taken from the noncontact topography images in Figure 4). The three plots in Figure 8 clearly show a sharp change in the deposited metal morphology starting at just below 3 EL. Taken together with the nc-AFM lattice images and IRS data (Figures 5 and 6), the picture emerges of a uniform accumulation of Al atoms below the SAM surface at the S/Au interface for up to ∼3 EL deposition followed by an abrupt transition to filament formation and overlayer nucleation and growth at higher coverages.

From the above morphology evolution trend and the shorting point distribution, we can speculate on the structural character of the filaments. Given the errors in estimating the actual surface areas of the individual shorted features (see above and ref 56), the number density plot (Figure 8b) is more useful for interpretations. In this plot, the ratio of the maximum number of short points per area ($\sim 3 \times 10^3\ \mu m^{-2}$ at ∼10 EL) to the SAM adsorbate molecule coverage is $\sim 6.5 \times 10^{-4}$ ($= 3 \times 10^3\ \mu m^{-2}/4.6 \times 10^6\ \mu m^{-2}$) or roughly 1 short point for every ∼1500 molecules. This sparseness of Al penetration to the substrate associated with shorted filaments formed at high deposited Al coverages strongly contrasts with the highly uniform penetration of Al atoms to the S/Au interface at ∼<3 EL coverages. This difference is consistent with filament formation in scattered static defects in the SAM. For purposes of a rough analysis we assume that the filament surface density at 10 EL represents the maximum static defect density. Since the static defects arise in an otherwise densely packed SAM [recall the lattice images on the bare SAM (Figure 2c) and that these SAMs are highly electrochemically blocking (data not shown)], it is likely that these defects are typically no larger than a single adsorbate lattice spacing in diameter (∼0.5 nm) on average. Correspondingly, given an ∼0.28 nm Al atom diameter, we bound the number of Al atoms that can fit laterally in a defect to 3 [packed triangularly with a 0.56 nm diameter, matching the smallest subunit of a FCC (111) surface plane]. For a defect depth equal to the SAM thickness (∼2.0 nm) the average total number of Al atoms per static defect thus would be ∼7−26, depending upon whether they stack as a single atom or offset three-atom triangles. From this the fraction of Al atoms at ∼10 EL coverage packed in filaments is $\sim(4.6-13.7) \times 10^{-4}$ [$=(7-26) \times (3 \times 10^3\ \mu m^{-2})/(10 \times 4.6 \times 10^6\ \mu m^{-2})$] or ∼0.05−0.17%, an extremely small fraction.

Finally, examining Figure 8c, the leveling off of the roughness trend at >5 EL shows that the Al atoms are beginning to nucleate uniformly across the surface to form continuous films. At this point one can expect an approach to a percolation threshold across the surface for the electrical current, consistent with the sharp increase in area of the short points (Figure 8a). In accordance, after repeated contact scans the area of short-circuit spots at the surface decreases as connecting paths across the surface between filaments are broken by the sweeping of the tip (see the Supporting Information).

3.2.5. Elimination of Shorts by Continued Exposure to Background Gas under Vacuum Conditions. For each freshly deposited sample with the chosen Al coverage, the total cp-AFM with simultaneous topography and current scans typically took ∼4 h and were carried out under a chamber pressure of $(1-5) \times 10^{-10}$ Torr. During the analysis time the electrical conduction data did not vary in terms of the electrical and spatial

(56) Because of the resolution of image (scan area, 1000 × 1000 nm; 256 sampling points per line), the geometry of the cp-AFM tip (radius ∼ 10−30 nm) and the torsional bending of the cantilever with undulation of surface topography, the diameter of current spots taken directly from the image are not accurate. Further, given the tip−surface contact area diameter of up to a few tens of nanometers, the AFM probe is not likely to be able to distinguish single from adjacent, closely spaced multiple filaments.

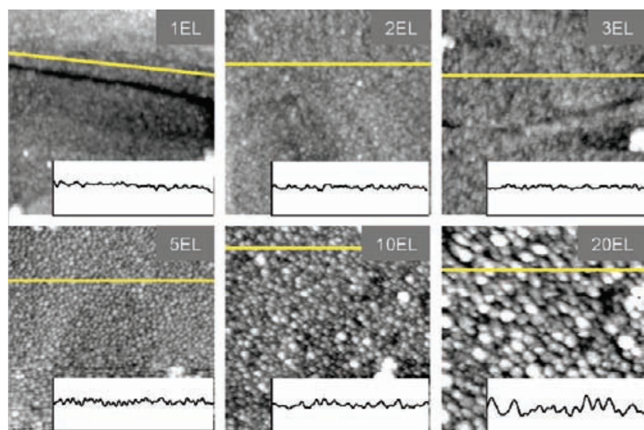

Figure 9. Topographic images (0.15 μm × 0.15 μm) of Al depositions at different coverages, as shown, on the ME-SAM taken by nc-AFM. Line scans are shown in the insets with full scale ± 2.5 nm.

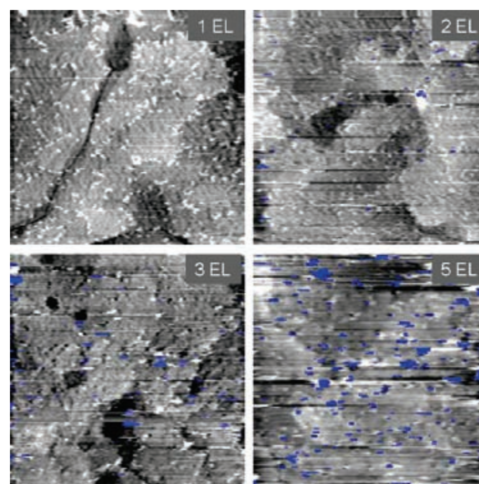

Figure 10. Topographic and current images (1 μm × 1 μm) of Al depositions at different coverages (shown on the images) on the ME-SAM. Current images are superimposed on the corresponding topographic images with the blue spots indicating points of short circuits (10 mV bias applied between the conducting probe and the Au substrate). The 2−5 EL images increasingly show some streaking due to the tip starting to sweep away some of the larger clusters which are easily dislodged.

characteristics once the initial effects of multiple tip scans and cluster sweeping were complete for the higher coverage samples (∼>3 EL). If the samples were left under vacuum for periods of ∼48 h or more, however, all electrical shorts vanished and the samples, even at high coverages (e.g., 5 EL), became fully insulating. From this we conclude that the presence of background oxidizing species, presumably mostly O_2, were able to oxidize the Al atoms embedded in filaments, thereby converting them to insulating forms of oxide, as well as convert some fraction of the surface metal overlayers to insulating oxide.

3.3. Al Deposition on the ME-SAM. 3.3.1. Evolution of Topography via Noncontact Mode Imaging. Comparison of the behaviors of the ME- and M-SAMs with Al deposition is important since the presence of the ME groups, according to our previous work, should completely block penetration into the SAM via chemical trapping, in contrast to profuse penetration for the M-SAM.[19] Topographic nc-AFM images (0.15 μm × 0.15 μm) of 1, 2, 3, and 5 EL of Al deposited on the ME-SAM (Figure 9) reveal that from the lowest Al coverage small clusters are observed across the entire surface and that the size of the clusters increases with the Al coverage, contrary to the present results of the M-SAM. As a more quantitative measure of cluster topography, rms roughnesses on the terraces of the M- and ME-SAMs as a function of Al coverage can be compared in Figure 8c. These results indicate a very high density of nucleation sites across the ME-SAM surface, consistent with the conclusions drawn previously from IRS spectroscopy of an ∼1:1 reaction of initially deposited Al atoms with the terminal ester groups.[19]

3.3.2. Formation of Electrical Shorts. Since our previous work showed that the nucleation of Al atoms on the ME-SAM is initiated by chemical reaction at the surface,[19] the formation of Al metal filaments via a dynamic penetration channel might not be expected. To check this aspect, simultaneous contact topographic and current mode images were taken. The images (1 μm × 1 μm) in Figure 10 show that no current above the noise level is observed at 1 EL Al, while only a few scattered spots appear for coverages ≥ 2 EL, in strong contrast to the extensive shorting on the M-SAM surface at the higher coverages, revealed clearly in Figure 8a,b.

There are two important aspects to note from these data: (1) the location of the filament short points at intrinsic defect regions in the SAM and (2) the apparent insulating character of the deposited 5 EL overlayer film. We discuss these in order.

First, note in Figure 10, particularly seen more clearly in the 2 and 3 EL coverages, the shorted spots dominantly occur at the edges of defect regions in the ME-SAM. These data strongly imply that penetration of free (unreacted) surface Al atoms to the substrate dominantly occurs through static defects in the SAM, and the subsequent flow of additional Al atoms leads to conducting filament growth. Note, however, that the number density of short points is far less for the ME-SAM than the M-SAM (Figure 8b) at the same total Al coverages. For example, at ∼3 EL deposition coverage the M- and ME-SAMs show average values of one short point for every 23000 and 3300 molecules, respectively. Three possible factors that can contribute to this difference are as follows: (1) partial blocking of static defect channels, as well as the dynamic channels, by the terminal -CO_2CH_3 trapping groups in the ME-SAM, (2) an increased number of static defects in the M-SAM due to lattice disordering effects of the S−Al−Au pinning layer, and (3) an increased number of electrical interconnections between short points in the M-SAM due to percolation through the deposited Al metal overlayer film. The latter factor can be discounted, however, particularly for the 3 EL deposition case, since the first ∼3 EL of Al deposited on the M-SAM penetrate dominantly to the Au/S interface region leaving only a minor fraction of Al atoms at the surface in the form of well-isolated clusters (see section 3.2.1).

Second, keeping in mind the points in the above paragraph, the data in Figure 10 support the conclusion that the Al overlayer film formed in the ME-SAM case behaves as an insulating dielectric material. Specifically consider the 5 EL Al coverage image. Given the chemical trapping of the terminal -CO_2CH_3 terminal groups, virtually all the Al atoms are in the overlayer, which amounts to ∼23 per nm^2 (=5 × 4.6/nm^2), equivalent to nearly two continuous Al metal monolayers formed with the standard areal density of ∼15 atoms/nm^2 for bulk metallic Al. Further, given the nearly atomically smooth character of the overlayer (see Figures 8c and 9), we conclude that the overlayer is highly continuous. Considering this structure, the most reasonable way to explain the presence of highly isolated short points (Figure 10) is for the overlayer Al film to be insulating.

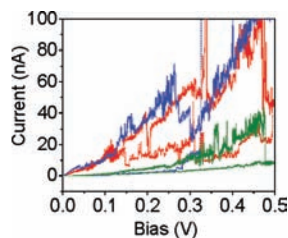

Figure 11. Current−voltage characteristics of 5 EL Al deposited M-SAM detected by randomly placed cp-AFM (Ir−Pt coating). The voltage is applied to the Au substrate, and the cp-AFM probe is grounded. Forward scanning (solid) and reverse scanning (dots) show hysteresis of current characteristics of the M−I−M molecular junction with hexadecane thiolate.

Otherwise, if the film were metallic it would be expected to act as a ground plane connected to the substrate via any connected filament, even one connected at a distant location from the tip contact point. This nonmetallic behavior of the initial 5 EL Al overlayer confirms our earlier conclusion of dielectric behavior, based on spectroscopic ellipsometry data.[19] At higher coverages the data showed the onset of a metallic film shorted to the substrate ground plane.

Finally, we note, consistent with the data for the M-SAM (section 3.2.5), that extended exposure of the 5 EL Al/ME-SAM deposition sample to the background gas in the analysis chamber ($\sim 5 \times 10^{-10}$ Torr) lead to loss of the shorting behavior and formation of a fully insulating film across the surface. Thus, the isolated Al filament conduction paths were eliminated, presumably via formation of an insulating oxide.

3.4. Electrical Characterization of Al Nanofilaments Formed in the M-SAM. 3.4.1. General Behavior of I−V Sweeps at 5 EL Al Coverage. To better characterize the electrical nature of the features responsible for electrical conductance in the M-SAM, a systematic series of single $I-V$ sweeps (increasing and decreasing back to zero bias) were made at large numbers of random points across the surfaces. Representative data for a 5 EL coverage surface (Figure 11) shows a variety of behaviors at the different points. At some the current is essentially at or near the noise floor (insulating spots) while others not only show current flow but show sudden changes in conductance during the voltage sweeps. Continued cycling was carried out at randomly selected points which exhibited multistable conductance behavior (see Supporting Information). In general, the behavior was erratic but some points showed memory behavior in which reverse bias sweeps reset the current state to one similar to the original value in the initial forward bias, while most point generally showed cycling for only one to three cycles before becoming insulating (fuse effect). Overall, in all the testing, a rich variety of behaviors were observed. The results were highly variable and unpredictable, categorized by characteristics such as fuse effects, switching, and memory.

3.4.2. Characterization of the Nanofilament Conductance Statistics at 5 EL Al Coverage. Further electrical measurements were made with careful control of the measurement conditions in order to probe in more detail the nature of the conductance channels on the surfaces of the 5 EL Al M-SAMs. A strategy was selected in which the cp-AFM probe was initially scanned across the surface twice at a consistent repulsive normal force loading of 5 nN before applying a bias for conductance measurements. This procedure was used to electrically isolate Al nanofilaments as much as possible by sweeping away larger surface clusters that could serve as electrical interconnections between different conduction channels. A typical current scan, at a 10 mV tip bias, of a twice swept surface is shown in Figure 12a (line scan for the yellow line is shown in the inset). On other freshly twice swept surfaces the current was measured at randomly selected spots with applied bias sweeps from 0 to 0.5 mV. For any given spot, when the current was below the detection limit ($\sim$1 pA) at the 0.5 mV point the spot was considered as insulating.

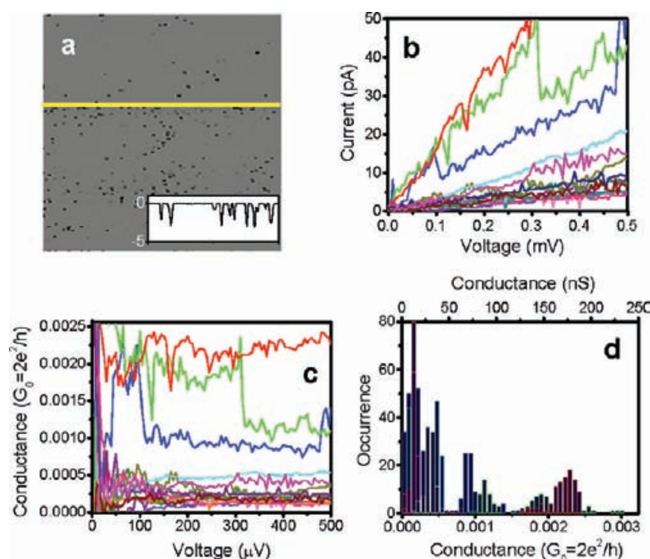

Figure 12. (a) Initial scan current image (1 μm × 1 μm) of a 5 EL Al deposited M-SAM taken by cp-AFM with an applied 10 mV test bias. A line scan (yellow line) is shown in the inset. (b) $I-V$ sweeps at random locations after two initial surface scans with an applied 5 nN normal force loading to the cantilever. Each 100 of the selected spot was probed with a 0−0.5 mV sweep. If the current at 0.5 mV was <1 pA, the point was considered insulating and the data were discarded for purposes of the statistics compilations. (c) Conductance of filaments directly calculated from the current−voltage characteristics in b with the y-axis in units of quantum conductance, $G_0 = 2e^2/h$ ($=77.5 \times 10^{-6}\ \Omega^{-1}$). (d) Distribution (occurrence) of conductance values taken from data points of the type of data shown in c. The distribution is calculated with a selected bin width of $6.5 \times 10^{-5}\ G_0$ ($5 \times 10^{-9}\ \Omega^{-1}$).

The single sweep data in Figure 12b generally show a linear type of $I-V$ relationship with a few scans showing sudden fluctuations, consistent with the cycling behavior in Figure 11. The corresponding Ohm's law conductances ($\langle G \rangle = \Delta I/\Delta V$) calculated directly from the averaged slopes of the plots in quantum conductance units ($G_0 = 2e^2/h = 77.5 \times 10^{-6}\ \Omega^{-1}$) are shown in Figure 12c. In general, the conductance values are independent of applied bias, except for the local fluctuations, and the absolute values are well below the quantum conductance limit for an ideal metal wire with no contact resistance. Further, the average values appear bunched into discrete ranges. The distribution of the conductance value ($\langle G \rangle$) from each of the $I-V$ sweeps (Figure 12c) is shown in Figure 12d with a selected bin width of $6.45 \times 10^{-5}\ G_0$ ($5 \times 10^{-9}\ \Omega^{-1}$). The plot reveals a tendency for $\langle G \rangle$ to bunch into groups, *very roughly* peaked near 0, 1, and $2 \times 10^{-3}\ G_0$, with the major contributions from the lower conductance range. Since the bin widths are significantly smaller than these peak distances, the distribution bunching is real.

This bunched conductance behavior is quite general. For example, Figure 13 shows representative conductance statistics (forward and reverse scan; 0−0.5 V bias) for randomly selected, multiple spots with roughly linear Ohmic responses across four different M-SAMs (a−d) with 10 EL coverages. The data were taken on the first AFM scan so that the surface features were

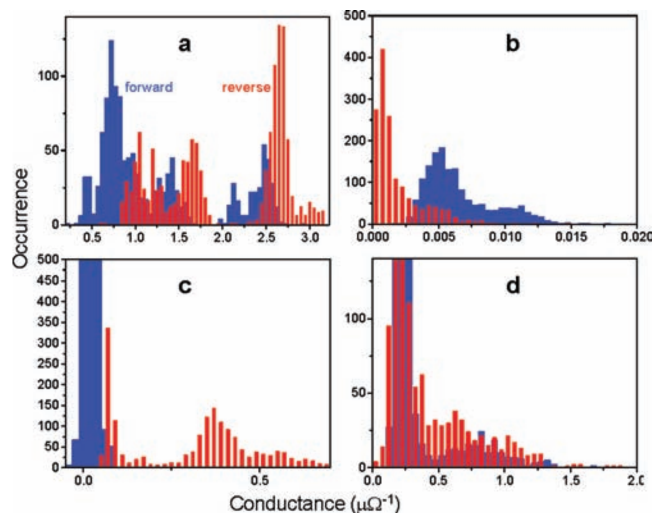

Figure 13. Conductance statistics for four representative M-SAMs with ~10 EL Al deposited. The data were taken on the first scan of the tip on the surface at multiple random spots with a 0−0.5 V forward (blue) and reverse (red) bias sweep at each measurement point. The analyses follow the protocol used for the data in Figure 11.

not preswept by the tip, thus leaving the clusters and topographical features intact for the measurements. Note the shifting of the responses between the collections of data on each sample and between forward and reverse scans on the same sample. At the high coverage (10 EL) the Al metal overlayer is highly interconnected so any random spot on the surface can provide contact to multiple filaments. This is manifested in the wide range of conductance values from spot to spot, far greater than the range observed in the preswept, 3 EL coverage samples (Figure 12) where the filaments are generally isolated.

4. Discussion

The AFM imaging data of the morphology evolution during Al deposition on the M- and ME-SAMs, in combination with IRS observations, not only confirm the previous conclusions inferred from spectroscopic data averaged over macroscopic surface regions[19] but add significant new conclusions with respect to the details of distinct morphology transitions and reveal the formation of Al nanofilaments with rich electrical properties. The discussion proceeds by first considering general thermochemical and kinetic aspects, then drawing conclusions on morphology and insulator−conductance transitions from the experimental data, and finally focusing on the interesting electrical properties of the nanofilaments formed in the M-SAM case.

4.1. Overall Thermochemical Considerations. One of the interesting aspects of the study of Al atom interactions with SAMs is the near complete lack of correlation of the final chemical state of the SAM with the overall thermochemical driving force from the ideal maximum change in chemical potentials. For quasi-solid-state systems such as the present ones, entropic changes generally can be ignored and the focus restricted to enthalpic changes. Using standard thermochemical data for heats of formation,[57] a simple analysis of the limiting extents of reaction possible at room temperature indicates that given a sufficient flux of Al atoms, both SAMs should react extensively to form inorganic products, including aluminum carbides, oxides (ME-SAM), hydrides, and sulfides. For example, consider a simple case in which for both SAMs the Al atoms "chew" off the top moiety of the SAMs, $-CH_3$ and $-CO_2CH_3$, as illustrated for the reactions that follow.

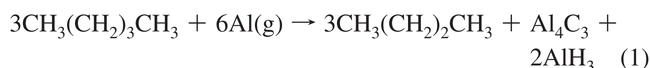

$$3CH_3(CH_2)_3CH_3 + 6Al(g) \rightarrow 3CH_3(CH_2)_2CH_3 + Al_4C_3 + 2AlH_3 \quad (1)$$

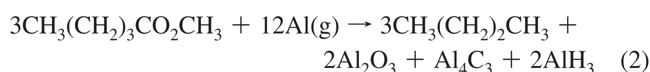

$$3CH_3(CH_2)_3CO_2CH_3 + 12Al(g) \rightarrow 3CH_3(CH_2)_2CH_3 + 2Al_2O_3 + Al_4C_3 + 2AlH_3 \quad (2)$$

In each case the reactions serve as model chemistry for the exhaustive reaction of the terminal groups with Al to form purely inorganic products with the remainder of the SAM terminated by formation of a C−H bond to form a terminal CH_3 group. For simplicity the ΔH_f° values were specified for the organic molecules and inorganic products in the condensed phase (liquids and solids, respectively), while Al atoms were set in the gas phase to match the conditions of isolated atoms on the surface. The corresponding heats of reaction are vigorously exothermic with $\Delta H_{298}^\circ = -741$ and -2161 kJ/(mol of alkane), respectively, for reactions 1 and 2. Some lowering of these energies would occur if the reactions were written in terms of Al dimers or clusters, but given the stabilizations of ~86.2 and 330 kJ·mol^{-1} of Al atoms in dimer and bulk solid form relative to the gas phase, respectively, the reactions of aluminum with the SAMs, however, remain significantly exothermic. On this basis one would predict that the vapor deposited Al atoms would exhaustively degrade the SAMs to inorganic products, similar to the processes that occur with Ti atoms deposited on the M-SAM.[30] In fact, it is notable that the final chemical state of the M-SAM with Al shows absolutely no evidence for attack of the Al atoms on the alkyl chain, but only a subtle insertion of a "monolayer" of Al atoms into the Au/S interface region with no continuing conversion to inorganic sulfide In line with this, even the efficiency of an impinging At atom adsorbing at the $-CH_3$ surface is low, ~40% as measured by the measured value of the sticking coefficient (*S*), which means that the energy accommodation of the metal atom by the surface is inefficient, allowing the excess kinetic energy to overcome van der Waals interactions and cause desorption.

On the other hand, for the ME-SAM, where a selective chemical reaction of the C=O moiety of the $-CO_2CH_3$ group occurs with high efficiency, it is striking that the highly exothermic path to form Al_2O_3 with complete degradation of the ester group does not prevail. Rather, from the present and our previous study,[19] there is no evidence for formation of the oxide and the degradation is so limited that the $-OCH_3$ group remains intact, as seen from IRS measurements.

Overall, these thermochemical considerations reveal the presence of large kinetic barriers to direct insertion of the Al surface atoms in the molecular bonds under our conditions of approximately room temperature SAMs and Al atoms arriving at the surface from a thermal deposition source. On this basis the final states of the SAMs must be viewed in terms of competing kinetic pathways involving both diffusion and chemical routes.

4.2. Overall Kinetic Pathways. For reference, Figure 14 shows generalized schematic representations of the major kinetic pathways for Al atom depositions onto terminal group functionalized alkanethiolate/Au SAMs. The rate constants for the most part represent global processes in which more than one elementary kinetic step is involved, e.g., multiple site hopping across the surface representing diffusion to a new location.

(57) http://webbook.nist.gov/chemistry/.

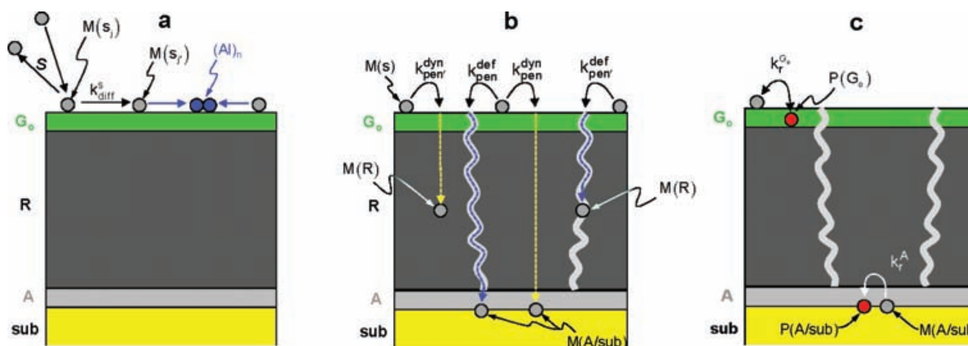

Figure 14. Schematics representing the generalized diffusion (a), penetration (b), and reaction (c) pathways relevant to the case of Al atom deposition onto the M- and ME-SAMs. Panel a shows collision of an Al atom at the vacuum interface with group G_0 with formation of an adsorbed surface atom at the location j [$M(s_j)$] followed by surface diffusion to arbitrary location j' with diffusion constant k^{s}_{diff} or scattering with overall sticking coefficient S. The right-hand side of the surface shows a binary collision of diffusing adsorbate Al atoms to form an aluminum dimer (blue circles), which in turn can be followed by additional collisions from other atoms to form an $(Al)_n$ cluster. Static defects in the SAM are not shown for simplicity since only surface diffusion processes are considered in this diagram. Panel b shows individual adsorbed surface atoms penetrating into the SAM via dynamically formed channels and static defects with associated rate constants $k^{dyn}_{pen.}$ and $k^{def}_{pen.}$. For generality, the penetration can lead to Al atoms embedded within the SAM matrix at trap sites [M(R)] or at the attachment group/substrate interface [M(A/sub)]. Panel c shows chemical reaction of a surface atom with a vacuum interface group to form product $P(G_0)$ (red circle). This reaction could consist, in general, of a simple complexation (van der Waals or salvation type of interaction) or an irreversible reaction to new products. The reaction arrow is shown as double sided to indicate that a weak solvation could be reversible, allowing the surface atom to continue diffusing. In the present case of G_0 = -CO_2CH_3 the reaction is irreversible. The scheme also shows reaction of an Al atom at the A/sub interface to form a product (red circle), understood from the present and previous results to be insertion of Al into the Au−S bond.

Collision of an Al(g) atom with the exposed SAM surface results in a stabilized adsorbate state at some location j at the vacuum interface [$M(s_j)$] or immediate recoil from the surface represented by a sticking probability S (Figure 14a). The high inertness of the Al atoms toward very energetically favorable chemical reactions in the case of the M-SAM is consistent with the observed value of $S \sim 0.4$; viz., over half of the surface collisions exhibit insufficient energy accommodation to result in sticking (in contrast, note that $S = 1.0$ for the reactive ME-SAM). Each adsorbed atom subsequently diffuses across the surface (represented by the generalized rate constant k^{s}_{diff}), undergoes penetration into the SAM via dynamic channels or static defects (represented by $k^{dyn}_{pen.}$ and $k^{def}_{pen.}$, respectively), or chemically reacts (or interacts) at various points (see Figure 14a−c). Complex morphological structures are not directly shown for brevity, but the evolution of these structures will arise by combinations of the simple kinetic processes; e.g., formation of metal clusters or nanofilaments would proceed by diffusion and nucleation of Al atoms or small clusters at some specific location such as the vacuum interface or in the interior of a SAM defect region. To be general, the reaction channels involving the SAM terminal groups are shown as reversible with a forward rate constant $k_r^{G_0}$ for formation of the product $P(G_0)$. An example of a reversible interaction comes from a previous study for the case of a terminal -OCH_3 group which shows that a weak solvation interaction can compete with penetration.[17,31]

4.3. Morphology and Electrical Conduction Transitions for Al Depositions on the M-SAM. 4.3.1. Morphology Transition with Al Coverage: Support for the Mechanism of Metal Atom Transport via Dynamically Formed Channels. The most striking feature of the evolution of structural characteristics with increasing Al atom deposition is the relatively abrupt transition, starting at ~3 EL and extending to ~5 EL, from a topographically smooth, translationally ordered, electrically insulating film to a comparatively rough surface with large Al clusters and a high surface density of electrical conduction paths to the substrate, as seen in Figure 8. Analysis of the topography image at ~3 EL Al (Figure 4) leads to a rough estimate that at the onset of this transition only ~0.1−0.5% of the deposited 3 EL Al is incorporated as nucleated clusters at the top surface of the SAM, consequently leaving the remaining >99% located within the SAM or in the S/Au interface region (see the Supporting Information). Given the tight packing of the SAM, even with decreases in the molecular tilt angles, there is insufficient free volume to contain 3 EL of Al within the SAM matrix without total disruption of the entire adsorbate lattice; therefore the metal atoms must be located in the interface region. The lattice images (Figure 5) of the 3 EL sample, taken after the surface clusters were swept away by the tip in contact mode, further indicate the metal distribution across the interface is remarkably uniform since the images show remaining vestiges of the original adsorbate ordering with very little increase in surface roughness. This structure is further supported by the very limited decay of the alkyl chain conformational order indicated by the IRS data in Figure 6. Thus, up to $\sim 3 \times 4.6 = 13.8$ Al atoms/nm^2 coverage the Al atoms appear to form a fairly uniform adlayer in the Au/S interface region. Above that coverage there is a distinct shift to growth of surface clusters of Al at the SAM/vacuum interface. Given that there are 13.8 Au atoms/nm^2 on a perfect (111) surface, the data show that the Al atoms approach a 1:1 Al:Au adlayer structure near the onset of a shift from penetration through the SAM to overlayer cluster formation at the SAM surface. An example of a possible limiting, ideal structure for the adlayer and overlayer SAM is shown in Figure 15. The top view (left) shows a (1−1) Al superlattice in registry with the hollow positions of the Au(111) underlayer, and the side view (right) shows a small subcell of the alkanethiolates set as a $(\sqrt{3} \times \sqrt{3}),R30°$ superlattice on the Al layer. Due to the lack of resolvable lattice structure from the AFM images, fine details of the actual structure cannot be discerned, although the observations of significant alkyl chain conformational ordering (IRS) and conservation of the adsorbate coverage do constrain the structure to maintain an arrangement consistent with an average adsorbate lattice spacing as for the initial $(\sqrt{3} \times \sqrt{3})$ SAM on Au(111). Overall, one would expect that an incompletely formed, imperfect adlayer would lead to a degradation of the $(\sqrt{3} \times \sqrt{3})$ lattice order for the SAM.

These data provide strong support for our previous speculation of Al atom penetration via transient defect channels arising from thermal fluctuations of the chains and their lateral positions

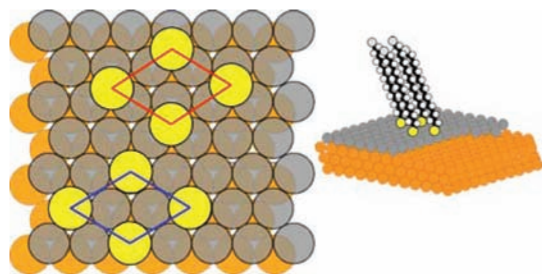

Figure 15. Schematics for a possible, ideal SAM−Al−Au layered structure formed by alkanethiolate molecule attachment to a (1 × 1) Al superlattice on Au(111) to form a ($\sqrt{3} \times \sqrt{3}$), *R*30° superlattice on the Al adlayer. The sulfur atoms (yellow circles) in the molecule subcell are shown on atop (blue lines) and 3-fold hollow (red lines) sites.

around the Au−S pinning sites.[31] In this mechanism the transient defect channels are formed randomly across the SAM, thereby leading to a uniform distribution of the penetrated Al atoms in the Au/S interface region. An important aspect of the mechanism is that Al atoms at this interlayer will insert into Au−S bonds to form Au−Al−S adsorbate attachment and that given the relatively larger bond strength of the Al−S bond, as concluded from our previous quantum chemical calculations,[31] it follows that increasing conversion of Au−S to Au−Al−S bonding would increasingly shut down the SAM penetration channel via freezing of the adsorbate positional fluctuations as the Al coverages approach a 1:1 Al/Au adlayer. The ∼3 EL threshold for the onset of top overlayer formation confirms this prediction.

In terms of kinetic competitions, the frequency of opening channels ($k^{\mathrm{dyn}}_{\mathrm{pen.}}$) must exceed the reactive collision frequency of Al atoms to form dimers. On the basis of a rough value of ∼300 meV (∼12 kT at 300 K) for the total hopping barrier of single thiolate molecules[58] diffusing across a Au(111) terrace and the lower value required for rocking slightly out of position in the pinning well, we estimate the time scale of the penetration channel opening to be roughly in the nanosecond or somewhat lower range. In comparison, assuming that isolated surface Al atoms behave as an ideal 2-D gas on a frictionless surface at 300 K, the isolated atoms would move over 10 molecules in ∼10 ps (∼300 $m \cdot s^{-1}$ speeds). Inclusion of hopping barriers of a few kilotesla would reduce this number into the nanosecond range. Thus, the time scales for opening of channels and arrival of atoms for entry is reasonable. Collision frequencies of isolated Al atoms to create Al dimers would depend second-order on the local surface coverages. Over ranges of possible surface coverages in the 1 EL integrated deposition range the collision frequencies should range in the nanosecond−picosecond time scales. The lack of a significant appearance of Al surface clusters definitively supports more rapid diffusion of Al atoms into penetration channels than across the surface to form $(Al)_n$ cluster species.

4.3.2. Insulator to Electrical Conduction Transition: The Role of Static Defects. A second, completely new aspect of the Al deposition mechanism the present study now reveals is the formation of electrically conducting Al nanofilaments, which begin to appear in the electrical measurements above ∼3 EL Al coverage (see Figure 8). Since the presence of nanofilaments does not appear until after the dynamic penetration channel closes down, we conclude that the nanofilaments are forming in static defects in the SAM. Further, since the lattice ordering has decayed somewhat at the ∼3 EL transition point, due to the formation of the imperfectly ordered S−Au−A interlayer, one can expect the presence of frozen defects (molecular scale "pinholes") to the limited extent allowed by the small total free volume in the SAM. From our previous study involving spectroscopic ellipsometry measurements we estimate that for the *n*-$C_{18}H_{37}$S-SAM on polycrystalline Au{111} the chains are packed at ≳80−92% of the theoretical surface density for the ($\sqrt{3} \times \sqrt{3}$) packing.[59] Since these polycrystalline substrates contain inherent roughness due to the presence of extensive grain boundaries, we expect that the corresponding Au/mica substrates with large (111) terraces used for our present AFM imaging would be significantly less defective prior to Al atom deposition. On this basis, we estimate that the intrinsic SAM defect content would be significantly <8%. Assuming cylindrical filament geometry with filament lengths roughly equal to the SAM thickness, the defect area thus would correspond to <8% of the total SAM geometric surface area. The data in Figure 8 provide two measures of this.

First, Figure 8a shows that on an areal basis an upper limit of ∼10% of the SAM surface is occupied by short-circuit points at ∼3 EL coverage, consistent with the above estimate. At higher coverages the short-circuit areas rise sharply, but we discount this as an accurate measure of nanofilament diameter since (1) at this point the Al atoms are depositing and forming nanoclusters at the surface which would make the apparent diameter of short-circuit points larger than the nanofilaments, (2) the number of electrical interconnections between the various short-circuit points is sharply increasing leading to a large area for electrical contact of the nanofilaments, and (3) the IRS data (Figure 6) indicate that no adsorbate molecules are being lost and thus the total free volume for static defects is small and constant. Second, Figure 8b shows ∼1.4×10^3 short-circuit points/μm^2 at 3 EL coverage, equivalent to ∼3×10^{-4} shorts/molecule or ∼1 short/(3300 molecules).

4.4. Surface Trapping of Al Atoms via Chemical Reaction with Terminal -CO_2CH_3 Groups in the ME-SAM. 4.4.1. Morphology Trends: Uniform Overlayer Nucleation and Growth. The behavior of the surface reactive ME-SAM serves as a useful reference for the case of unreactive M-SAM. In particular, by ∼1 EL deposition each Al atom has reacted with a terminal -CO_2CH_3 group of the ME-SAM, thereby effectively preventing penetration into the SAM, i.e., $k^{\mathrm{ester}}_{\mathrm{r}} \gg (k^{\mathrm{dyn}}_{\mathrm{pen.}}, k^{\mathrm{pen.}}_{\mathrm{dyn}}, k^{\mathrm{s}}_{\mathrm{diff}})$, in complete contrast to the case of the M-SAM where the dynamic penetration channel is nearly exclusive at 1 EL. Further, for increasing coverages the growing overlayer on the ME-SAM remains quite smooth and uniform (rms roughness ≲0.1−0.2 nm), again in contrast to the M-SAM where the onset of overlayer growth near ∼3 EL results in cluster formation and relatively rough surfaces with rms roughness approaching ∼2 nm at 20 EL.

4.4.2. Electrical Properties. The most important aspect of the electrical behavior for the ME-SAM is that the overlayer Al film remains almost completely insulating with increasing Al deposition up to ∼5 EL. The electrical current images reveal that even at ∼5 EL the electrical shorting points across the surface are quite isolated, occupying only a few percent or less of the total area, consistent with an insulating character of the overlayer. This conclusion directly confirms our earlier indirect conclusion, based on spectroscopic ellipsometry measurements

(58) For example, see: Mahaffy, R.; Bhatia, R.; Garrison, B. J. *J. Phys. Chem. B* **1997**, *101*, 771−773.

(59) Shi, J.; Hong, B.; Parikh, A. N.; Collins, R. W.; Allara, D. L. *Chem. Phys. Lett.* **1995**, *246*, 90–94.

in the ∼1−5 eV range, of a dielectric (wide bandgap) overlayer up to a coverage of ∼5 EL of Al.[19] The detailed chemical and structural character of this overlayer remains uncertain, e.g., the valence states of the Al atoms and the incorporation of Al−O bonding, and further work is needed to resolve this issue.

The second important aspect is that the Al filaments appear to form dominantly at the edge of static surface defects in the SAM (with rates consequently controlled by $k_{\text{pen.}}^{\text{def}}$). The observation of shorting points in the insulating ∼5 EL overlayer film indicates that the filament growth continues during the growth of the insulating dielectric overlayer up to the 5 EL coverage. The significantly lower surface density of shorting points for the ME-SAM relative to the M-SAM (see Figure 8) is interesting to note given that one might expect the M-SAM film, with the small nonpolar terminal -CH_3 group, to form a more ordered structure with fewer static defects than the ME-SAM with the bulkier, polar -CO_2CH_3 group. In the case of the M-SAM, however, the preformation of the ∼3 EL Al underlayer at the Au−S interface with resultant imperfections and strain can be expected to create new static defects, thus providing additional regions for Al filament growth. Since there is no underlayer film in the ME-SAM case, one can presume that the shorting point distribution follows the intrinsic static defect distribution in the pure SAM.

4.5. Electrical Conductance Properties and Associated Statistics of Al Nanofilaments in the M-SAM. The CP-AFM data collected on a large number of random spots across the M-SAM surfaces at 3 EL coverage (Figure 12) show a variety of electrical behaviors, including switching and memory. A number of other data were gathered as well at different coverages over a large number of spots (e.g., Figure 13) which follow similar behavior modes. Taking the general conclusions and estimates from the topographic and electrical data that an average nanofilament consists of no more than ∼20−30 Al atoms, it is not surprising that this variable behavior occurs under electrical bias sweeps of 0−0.1 or 0.5 V applied over only ∼2 nm distances, giving voltage gradients in the range of $\sim 10^8\ \text{V}\cdot\text{m}^{-1}$.

In general, statistical analysis of the data from multiple samples and contact points across the surface shows a strong tendency for bunching of the conductance values into a pattern of stepped ranges. The values associated with single filaments (Figure 12) are several orders of magnitude less than the quantum conductance limit but do appear very roughly to bunch with integral jumps reminiscent of quantum controlled conductance. While these data are insufficiently precise to merit deep interpretation at this point, they do appear to signal some fundamental behavior of strings of Al atoms. The electronic behavior of atomic-sized conductors has been a longstanding problem of interest with theoretical[60−63] study and more recently a variety of experimental approaches, including STM point contact measurements,[63−68] mechanically controlled break junctions,[69] and e-beam assisted thermal migration.[70] Low conductance values in nanojunctions have been of interest and interpreted in terms of factors including contact resistance,[61,62] scattering effect of imperfect wire,[61,62,64,65,69] geometrical factors (length, angle of edge, etc.),[62,71−73] impurities,[61,62,74,75] longitudinal potential distribution,[61,62,76] Fermi-level smearing,[62] and Fermi-level localization in the junction.[77] For our case of the Al nanowires the observed subquantum limit conductances with bunching of values suggest that factors such as contact resistance and nanofilament defects are operative (e.g., short nanofilaments leaving tunneling gaps to the conducting AFM tip and/or the substrate plane).[61,62,70−73,77−80] These effects, combined possibly with more fundamental effects, can diminish the conductance values while leaving vestiges of quantum conductance gaps. Further work is needed to resolve these issues.

From a more practical point of view with respect to molecular electronic devices, the junction shows the problems that can arise in fabrication of these types of devices using metalized top contacts in metal/molecule/metal junctions. The formation of even traces of metal nanowires during top metal deposition can lead to a range of highly erratic, unfavorable device behaviors, e.g., fluctuating switching, Ohmic conduction, and memory, with consequent domination over a desired device behavior derived from the intrinsic electrical properties of the molecules. On the other hand, if one were able to reproducibly make structures with narrowly controlled effects, it might be possible to derive useful device behaviors. An interesting view of this in terms of an emerging class of memory device operation based on Ohmic resistance changes involving nanoscale restructuring (*memristor*) has been recently discussed in an intriguing paper by Williams and co-workers.[81] On this basis the ability to apply high control to the formation of nanofilaments provides a unique way to the fabrication of new classes of devices at the molecular scale.

5. Conclusions and Future Work

Topographical, electrical, and vibrational spectral features have been obtained using in situ AFM and IRS for controlled coverage vapor deposition of Al onto methyl- and methyl ester-terminated hexadecanethiolate SAMs on Au{111} substrates.

(60) Landauer, R. *IBM J. Res. Dev.* **1957**, *1* (3), 223–231.
(61) Agrait, N.; Yeyati, A. L.; van Ruitenbeek, J. M. *Phys. Rep.* **2003**, *377* (2−3), 81–279.
(62) Tekman, E.; Ciraci, S. *Phys. Rev. B* **1991**, *43* (9), 7145.
(63) Besenbacher, F. *Rep. Prog. Phys.* **1996**, *59* (12), 1737–1802.
(64) Olesen, L.; Laegsgaard, E.; Stensgaard, I.; Besenbacher, F.; Schiøtz, J.; Stoltze, P.; Jacobsen, K. W.; Nørskov, J. K. *Phys. Rev. Lett.* **1994**, *72* (14), 2251–2254.
(65) Olesen, L.; Laegsgaard, E.; Stensgaard, I.; Besenbacher, F.; Schiøtz, J.; Stoltze, P.; Jacobsen, K. W.; Nørskov, J. K.; Olesen, N/A *Phys. Rev. Lett.* **1995**, *74* (11), 2147.
(66) Ohnishi, H.; Kondo, Y.; Takayanagi, K. *Nature* **1998**, *395* (6704), 780–783.
(67) Yanson, A. I.; Bollinger, G. R.; van den Brom, H. E.; Agrait, N.; van Ruitenbeek, J. M. *Nature* **1998**, *395* (6704), 783–785.
(68) Lang, N. D. *Phys. Rev. B* **1987**, *36* (15), 140–143.
(69) Muller, C. J.; van Ruitenbeek, J. M.; de Jongh, L. J. *Phys. Rev. Lett.* **1992**, *69* (1), 140.
(70) Rodrigues, V.; Fuhrer, T.; Ugarte, D. *Phys. Rev. Lett.* **2000**, *85* (19), 4124–4127.
(71) de Heer, W. A.; Frank, S.; Ugarte, D. *Z. Phys. B: Condens. Matter* **1997**, *104* (3), 469–473.
(72) Jelinek, P.; Perez, R.; Ortega, J.; Flores, F. *Phys. Rev. B* **2003**, *68* (8), 085403.
(73) Skorodumova, N. V.; Simak, S. I.; Kochetov, A. E.; Johansson, B. *Phys. Rev. B* **2005**, *72* (19), 193413–193414.
(74) Brandbyge, M.; Jacobsen, K. W.; Norskov, J. K. *Phys. Rev. B* **1997**, *55* (4), 2637–2650.
(75) Untiedt, C.; Bollinger, G.; Vieira, S.; Agrait, N. *Phys. Rev. B* **2000**, *62* (15), 9962–9965.
(76) Louis, E.; Vergas, J. A.; Palacios, J. J.; Perez-Jiminez, A. J.; SanFabian, E. *Phys. Rev. B* **2003**, *67* (15), 155321-1–155321-5.
(77) Yeyati, A. L.; Martin-Rodero, A.; Flores, F. *Phys. Rev. B* **1997**, *56* (16), 10369–10372.
(78) Sirvent, C.; Rodrigo, J. G.; Vieira, S.; Jurczyszyn, L.; Mingo, N.; Flores, F. *Phys. Rev. B* **1996**, *53* (23), 16086–16090.
(79) Verstraete, M. J.; Gonze, X. *Phys. Rev. B* **2006**, *74* (15), 153408–153414.
(80) Engelkes, V. B.; Frisbie, C. D. *J. Phys. Chem. B* **2006**, *110* (20), 10011–10020.
(81) Strukov, D. B.; Snider, G. S.; Stewart, D. R.; Williams, R. S. *Nature* **2008**, *453*, 80–83.

In spite of large thermochemical driving forces to form inorganic products with complete degradation of the SAMs, the products are formed by subtle, kinetically controlled channels involving competitions between surface clustering, penetration into the SAM Au−S underlayer, via static and dynamic processes, and highly selective, limited chemical reaction at the surface.

The M-SAM case is dominated by a preliminary path in which Al atoms penetrate to the via a dynamic channel involving lateral fluctuations of the adsorbate molecule positions with the penetration closing down after ∼3 Al atoms/molecule or ∼1 Al/Au in the substrate surface layer. In parallel, isolated Al metal nanofilaments consisting of nanometer-scale strings of atoms form at static defects and exhibit a statistical distribution of electrical conductances with bunched values, reminiscent of quantum conductance behavior, and with varied bias voltage responses ranging across linear Ohmic conduction, switching, and memory. Past the 3 Al atoms/molecule coverage additional deposited Al atoms nucleate to form overlayer clusters and eventually a continuous electrically conducting film. The ME-SAM case, in contrast, involves near quantitative 1:1 reaction with the ester groups initially, followed by deposition of 4 more Al atoms/molecule to form a smooth uniform, electrically insulating overlayer with the appearance of highly isolated filaments across the surface formed at static SAM defects. Since the overlayer is not inorganic aluminum oxide, it must consist of some type of organoaluminum species with insulating properties. Determining the structure would be greatly aided by quantum chemical theory calculations, and such work is underway in our laboratory.

Taken together, these results illustrate the rich behavior of metal atom−SAM interactions guided dominantly by subtle kinetic pathways in spite of high thermochemical driving forces. The effects of sample temperature in shifting the competing pathways are of interest and experiments are in progress in this direction. Overall, the inability to control the subtleties in these systems can provide serious challenges for technological applications such as metallization for top contacts in molecular electronic devices using SAMs and thin organic films, while in contrast, the ability to provide control offers potential opportunities to fabricate new types of devices which could operate via designed nanofilaments as well as provide new types of atomic-scale structures for fundamental research in quantum conduction. Experiments along these directions are now in progress in our laboratory.

Acknowledgment. The authors acknowledge funding from ONR, ARO (MURI on Nanoenergetic Materials), and NSF (Pennsylvania State University MRSEC Grant No. DMR-0080019).

Supporting Information Available: Tip degradation, short-circuit current time dependence, switching and conductance characteristics of filaments, and fractions of Al in underlayer, filaments, and overlayers. This material is available free of charge via the Internet at http://pubs.acs.org.

JA901376W